Chapter 4

Nonlinear modelling of shoreface–connected sand ridges.

As an extension of the model discussed in the chapter 2 of this thesis, a nonlinear stability analysis is applied to investigate the long-term behaviour of finite-amplitude shoreface-connected sand ridges. These bedforms are trapped on the inner shelf, have alongshore spacings of $5-8$ km and the crests form an oblique angle with the coast. The basic model consists of the 2DH shallow water equations, a local sediment transport parametrization and a bottom evolution equation. This model allows for a basic state which describes a steady alongshore uniform flow over the inner shelf. The instability of this flow with respect to bottom perturbations, as triggered by the transverse shelf slope, causes the formation of ridges of which the initial behaviour is described by linearized equations.

The studies of chapter 2 and Trowbridge (1995) are both linear stability analyses. They yield information about the growth rate, migration speed and spatial patterns of the bottom modes. In chapter 2 we even predict a most preferred mode, which has the largest growth rate, by incorporating the effect of the bed slope in the sediment transport. A serious limitation of linear stability analyses is that they only describe the initial formation of the bed forms. The reason is that the amplitudes are assumed to be infinitesimally small, such that nonlinear terms can be discarded. However, if there exist modes with positive growth rates, after some time their amplitudes will become so large that nonlinear terms become important: there will be mode competition. Previous studies on nonlinear morphodynamics (e.g. Blondeaux 1990; Vittori & Blondeaux 1990, 1992 on sea ripples, Colombini *et al.* 1987; Schielen *et al.* 1993 on river bars or Schuttelaars 1998 on tidal embayments) have demonstrated that this can result in complex behaviour of bed forms, such as amplitude modulation, multiple attractors and aperiodic solutions. There is no a priori reason that the long-term dynamics is dominated by the linearly most favourable modes, although this is what is observed in most nonlinear morphologic models. Also the flow pattern induced by finite-amplitude ridges may be substantially different from that observed during the initial growth stage.

The objective of the present chapter is to extend the models of chapter 2 and Trowbridge (1995) into the nonlinear regime and use the full model to study the long-term, finite-amplitude behaviour of the ridges. In particular results on the characteristic amplitudes of the bed forms, the feedback to the net currents, and the existence of multiple equilibria as well as periodic and aperiodic behaviour will be presented. Furthermore, it will be shown that in this model for realistic parameter values the long-term behaviour is not dominated by the linearly most preferred mode.

The nonlinear behaviour is computed by expanding the flow and bottom in eigenfunctions of the linear problem and appears to be controlled by the bed slope coefficient γ in the sediment transport. For large γ only one mode initially has a positive growth rate and solutions tend to finite-amplitude ridges, with an amplitude proportional to $(\gamma^{-1} - \gamma_c^{-1})^{1/2}$. For smaller γ more modes initially grow and the dynamics is no longer dominated by the linearly most preferred mode. In this regime quite a large number of eigenfunctions are required to obtain reliable solutions. As a result multiple attractors are found and even aperiodic behaviour is observed. Typical amplitudes
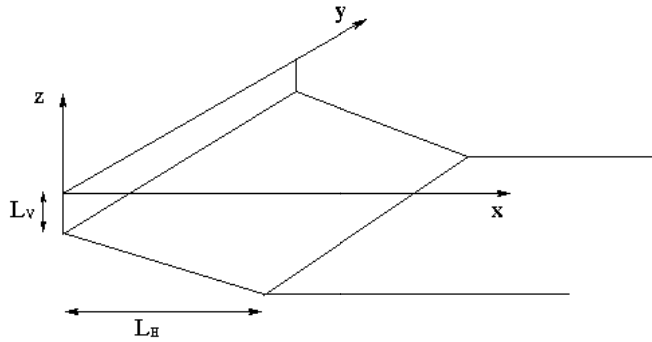
Figure 4.1: Sketch of the geometry and the coordinate system. For explanation of the symbols see the text.

and corresponding bottom and flow patterns correspond quite well with observations.

In the next section the model will be presented, followed by a discussion of the basic state and formulation of the perturbed model in sections 4.2.1 and 4.2.2, respectively. In section 4.2.2 the linear and the non–linear models are formulated, the main results of the linear stability analysis are summarized, and the truncation of the system is discussed. Next, in section 4.3 the nonlinear model set-up is discused by expanding the solutions in eigenfunctions of the linear problem. In section 4.4 the final the conclusions are given.

4.1   Governing equations. Scaling

Results of chapter 2 and 3 have shown that a model consisting of the 2DH shallow water equations with the friction and sediment tranport varying linearly with velocity and a steady basic velocity driven by a longshore pressure gradient is able to reproduce the main characteristics of the shoreface–connected sand ridges. The nonlinear stability analysis discussed iin this chapter is also based on this model. The model presented in section 2.1 of chapter 2 is reproduced in this section for the case of linear friction and sediment transport varying linearly with velocity. An extended and detailed discussion can be found there.

The fluid motion is considered to be governed by the depth-averaged momentum equation and mass conservation equation. The bottom evolution follows from the sediment conservation equation. An orthogonal coordinate system (figure 4.1) is taken with the x, y and z-axes pointing in the cross–shore, longshore direction and vertical direction, respectively. The still water level is represented by $z = 0$.

In order to make the equations of motion (2.1), (2.2) and (2.3) dimensionless we introduce characteristic magnitudes L_H, L_V and U for the horizontal length, the depth and the current. L_H is the width of the inner shelf, L_V and U are typical values of the water depth and the mean current. The variables are made dimensionless as follows:

$$(x, y) \rightarrow L_H (x, y) \qquad z_b \rightarrow L_V z_b \qquad \boldsymbol{v} \rightarrow U \boldsymbol{v} \qquad t \rightarrow T_m t \qquad z_s \rightarrow \frac{U^2}{g} z_s \,.$$

where T_m is a morphological time scale that will be defined below. Free surface elevation is scaled from the balance between the advection and the presure gradient terms. For example, representative values for the Dutch inner shelf are $L_H \sim 12 \times 10^3$ m, $L_V \sim 15$ m and $U \sim 0.25$ m s^{-1}. The scaled momentum and mass conservation equation read:

$$\epsilon \partial_t \boldsymbol{v} + (\boldsymbol{v} \cdot \boldsymbol{\nabla}) \boldsymbol{v} + \hat{\boldsymbol{f}} \times \boldsymbol{v} = -\boldsymbol{\nabla} z_s + \frac{\tau}{D} \tag{4.1a}$$

$$\epsilon \partial_t D + \boldsymbol{\nabla} \cdot (D \boldsymbol{v}) = 0 \tag{4.1b}$$

and the sediment conservation equation read:

$$\partial_t z_b + \boldsymbol{\nabla} \cdot \boldsymbol{q} = 0 \,. \tag{4.2}$$

where $\epsilon = T_h/T_m$ is the ratio of the hydrodynamic time scale to the morphological one. Here $\boldsymbol{v}$ is the current vector, $\hat{\boldsymbol{f}} \times \boldsymbol{v}$ is the Coriolis acceleration, $\boldsymbol{\tau}$ represents the free surface and bottom stress terms ($\boldsymbol{\tau} = \boldsymbol{\tau}_s - \boldsymbol{\tau}_b$). The free surface, the bottom and the total height of the water column are given by $z = z_s$, $z = z_b$ and $D = F^2 z_s - z_b$, where F the Froude number ($F^2 = U^2/g\,L_V$). The volumetric sediment flux per unit width is denoted by $\boldsymbol{q}$. By performing the scaling of the equations, two time scales appear: a hydrodynamical one, T_h, from the scaling of the three flow equations (4.1) and a morphological one, T_m, from the scaling of the bottom evolution equation (4.2). They are defined as

$$T_h = \frac{L_H}{U} \qquad\qquad T_m = \frac{L_H L_V}{\nu U}$$

The constant ν is the proportionality coefficient between the sediment flux, $\boldsymbol{q}$, and the mean current. It depends on the wave stirring and on the sediment properties and bed porosity, but it has been assumed to be constant in this study. Thus, it is incorporated in the scaling and the non dimensional sediment transport parametrization is then written as

$$\boldsymbol{q} = |\boldsymbol{v}| \left(\frac{\boldsymbol{v}}{|\boldsymbol{v}|} - \gamma \boldsymbol{\nabla} h \right) . \tag{4.3}$$

The term $-\gamma \boldsymbol{\nabla} h$ accounts for the tendency of sand to move downslope, where h is the elevation of the bottom with respect to a specific equilibrium profile to be discussed in the next sections. In linear stability analysis performed in chapter 2, shoreface–connected ridges were found for the case that the sediment transport was linear in the velocity, which applies to stormy conditions. It motivates the choice of a sediment transport which is linear in the mean current. From the same analysis, a linear friction law $\boldsymbol{\tau}_b = r\boldsymbol{v}$ will be considered. The relation between the dimensional Coriolis, frictional and bed slope parameters, f_c, r_*, γ and their non-dimensional counterpart reads

$$\hat{f} = f_c \frac{L_H}{U} = Ro^{-1} \qquad\qquad r = r_* \frac{L_H}{U L_V} \qquad\qquad \hat{\gamma} = \gamma \frac{L_V}{L_H}$$

Using the scales of motion and assuming the hydrodynamic timescale much smaller than the morphological one, it appears that the Froude number can be neglected ($F = 0$) and that the quasi-steady hypothesis can be assumed ($\epsilon = 0$). See chapter 2 for an extended discussion of the parameter values. It is important to note that, since the growth of the ridges takes place on very long time scales ($O(10^3$ yr)), all the quantities in the governing equations have to be considered as averages over a long time ($O(10$ yr)).

The boundary conditions imposed for this system are periodic conditions in the longshore direction. At the transition shoreface-inner shelf and far offshore we assume that the cross-shore flow component vanishes and the bottom elevation is fixed to its reference value.

The formation and evolution of rhythmic bed forms will be investigated in the following sections by studing the dynamics of pertubations (u, v, η, h) evolving on a steady state $(0, V, \zeta, H)$:

$$\begin{aligned}
\boldsymbol{v} &= (0, V) + (u(x, y, t), v(x, y, t)) \\
z_s &= \zeta + \eta(x, y, t) \\
z_b &= -H + h(x, y, t)
\end{aligned} \tag{4.4}$$

4.2 Stability analysis

4.2.1 Basic state

Field observations of the bathymetry of the inner shelf indicate that the mean bottom profile (ie., averaged in the longshore direction) is characterized by a nearly constant slope. The slope of the outer shelf is considerably smaller. In this study we model the reference bottom profile as

$$H(x) = \begin{cases} 1 + \beta x & (0 \le x < 1) \\ 1 + \beta & (x \ge 1) \end{cases} .$$

Note that $H(x)$ and x are dimensionless and that the depth at the seaward end of the shoreface has been chosen as vertical length-scale, L_V. In case of the Dutch inner shelf, $L_V \sim 15$ m, $L_H \sim 12 \times 10^3$ m and the water depth on the outer shelf is approximately 20 m , so that $\beta = 0.33$.

As a consequence of the analysis done in chapter 2 we neglect the effect of the surface wind stress and we will consider a steady mean longshore current with a cross-shore gradient, $V(x)$, which is driven by a uniform mean longshore gradient in the free surface elevation, s. This velocity profile is equivalent to the one in chapter 2 with $a = 1$. This would mean a basic steady state of the form

$$\boldsymbol{v} = (0, V(x)) \qquad\qquad z_s = \delta\, y + \xi(x) \qquad\qquad z_b = -H(x)$$

where $\delta = g\, s\, L_H / U^2$ is the dimensionless parameter for the longshore gradient in the sea surface, s.

The momentum equations (4.1a) for this reference state read

$$\hat{f}\, V = \frac{\mathrm{d}\xi}{\mathrm{d}x}\,, \qquad\qquad\qquad 0 = \delta + \frac{r\, V}{H}\,.$$

A velocity profile given by $V = -(\delta/r)\, H$ obeys the alongshore momentum balance between forces related to the longshore pressure gradient and bottom friction. The mass conservation equation (4.1b) is verified identically and, since $h = 0$, the sediment flux (4.3) is directed alongshore and there are no spatial divergences in the transport. Now define the velocity scale U such that $|V|(x = 0) = 1$. This yields $r = \delta$ and using the expression for the reference bottom results in the velocity profile

$$V(x) = \left\{ \begin{array}{ll} \pm(1 + \beta\, x) & \text{if } 0 \le x \le 1 \\ \pm(1 + \beta) & \text{if } x > 1 \end{array} \right. \;.$$

The sign of the flow is determined by the direction of the applied longshore pressure gradient forces: δ is negative in case $V > 0$. Assuming that $r_* = c_d\, U$ and a drag coefficient of the bottom $c_d \simeq 0.002$, and a velocity scale of approximately $0.25\ \mathrm{m\,s^{-1}}$, the sea surface slope will be $s \sim 8 \times 10^{-7}$. This surface slope will induce over a distance of $100\ \mathrm{km}$ a free surface elevation difference $\Delta z_s \sim 0.1\ \mathrm{m}$.

4.2.2 Perturbed equations

The perturbed momentum, mass and sediment conservation equations for the perturbed state (4.4), discussed in section 4.1, read:

$$0 = V\partial_y u + (u\partial_x + v\partial_y)u - \hat{f}v + \partial_x\eta + \frac{r u}{H - h} \tag{4.5a}$$

$$0 = V\partial_y v + uV_x + (u\partial_x + v\partial_y)v + \hat{f}u + \partial_y\eta + \frac{r v - \delta h}{H - h} \tag{4.5b}$$

$$0 = H_x u + H\partial_x u - \partial_x(uh) + H\partial_y v - V\partial_y h - \partial_y(vh) \tag{4.6}$$

$$\partial_t h = -\boldsymbol{\nabla} \cdot (\boldsymbol{v} - \gamma|\boldsymbol{v}|\boldsymbol{\nabla}h) \tag{4.7}$$

with $|\boldsymbol{v}| = (V^2 + 2Vv + u^2 + v^2)^{1/2}$.

Equations (4.5), (4.6) and (4.7) can symbolically be written as:

$$\mathcal{S}\Phi_t = \mathcal{L}\Phi + \mathcal{N}(\Phi) \tag{4.8}$$

where $\Phi = (u, v, \eta, h)$. The subscript t denotes differentiation with respect to the time, the matrix $\mathcal{S}$ is given by

$$\mathcal{S} = \begin{pmatrix} 0 & 0 & 0 & 0 \\ 0 & 0 & 0 & 0 \\ 0 & 0 & 0 & 0 \\ 0 & 0 & 0 & 1 \end{pmatrix}$$

whereas $\mathcal{L}$ and $\mathcal{N}(\Phi)$ are the linear operator and the non–linear operator with the higher than linear terms of (4.5)–(4.7), respectively.

Linear analysis: formulation

The stability of the basic state discussed in 4.2.1 can be studied by considering the evolution of small perturbations. They can symbolically be written as:

$$\mathcal{S}\Phi_t = \mathcal{L}\Phi$$

Because of the structure of these equations and the boundary conditions in the longshore direction, we will consider alongshore travelling and growing wave solutions of the form

$$\Phi(x,y,t) = \Psi_{kn_k}(x,y)e^{\omega_{kn_k}t} \qquad \text{where } \Psi_{kn_k}(x,y) = \psi_{kn_k}(x)e^{iky}$$

and $\psi_{kn_k}(x) = (u(x), v(x), \eta(x), h(x))_{kn_k}$. Then, for each alongshore wavenumber k and cross-shore modenumber n_k, an eigenvalue problem is obtained to determine ω_{kn_k} and $\psi_{kn_k}(x)$,:

$$\omega_{kn_k}\mathcal{S}\psi_{kn_k} = \mathcal{L}_k\psi_{kn_k}$$

The solution of this eigenvalue problem yields for each k a spectrum of eigenvalues ω_{kn_k} ($n_k = 1, 2, 3, ...$) with their eigenfunctions, Ψ_{kn_k}. The eigenvalue ω_{kn_k} is a complex number, $\text{Re}(\omega_{kn_k})$ denotes the growth rate and $-\text{Im}(\omega_{kn_k})/k$ is the migration speed of the perturbations, in particular of the bed forms. Note that the eigenfunctions of the linear problem (normal modes) are two-fold; k referring to the longshore structure of the solution and, for each k, n_k referring to the cross-shore structure. Because eigenvalues will be sorted by their real part, n_k also refers to the relative value of the growth rate of ω_{kn_k}.

For each k, the linear operator can be rewritten as:

$$\mathcal{L}_k = \begin{pmatrix} ikV + \dfrac{r}{H} & -\hat{f} & \dfrac{\mathrm{d}}{\mathrm{d}x} & 0 \\[2ex] V_x + \hat{f} & ikV + \dfrac{r}{H} & ik & -\dfrac{\delta}{H} \\[2ex] H_x + H\dfrac{\mathrm{d}}{\mathrm{d}x} & ikH & 0 & -ikV \\[2ex] -\dfrac{\mathrm{d}}{\mathrm{d}x} & -ik & 0 & \gamma|V|(\dfrac{V_x}{V}\dfrac{\mathrm{d}}{\mathrm{d}x} + \dfrac{\mathrm{d}^2}{\mathrm{d}^2x} - k^2) \end{pmatrix}$$

The pertinent boundary conditions are that u and h should vanish at $x = 0$ and $x \to \infty$ for each solution $k\,n_k$. As in chapter 2, in the discretization of the cross–shore direction a collocation method has been used. For good precision in spatial structure of the eigenfuctions $\psi_{kn_k}(x)$ more than 60 collocation points are needed.

Linear stability analysis: results

Before dealing with the nonlinear equations, it is convenient to briefly summarize the main results of the linear stability analysis. A detailed description can be found in chapter 2. The choice of the parameter values has already been discussed in section 4.2.1 and are representative for the inner shelf along the central Dutch coast.

In figure 4.2 the growth rates of the perturbations are shown as a function of the longshore wavenumber for different cross-shore modes (mode numbers $n_k = 1, 2, 3$). Clearly, growth rates are positive for a broad spectrum of perturbations, hence there is a positive feedback between the water motion and bed forms. Furthermore, the growth rate curve of each cross-shore mode attains a maximum. The corresponding wavenumber is that of the perturbation which is initially most preferred. For $\gamma = 1.0 \times 10^{-4}$ the maximum growth rate corresponds to an e-folding timescale of approximately 5000 yr and the longshore wave-length of the most preferred bed form is about 8 km. The migration speed appears to be rather insensitive to the wavenumber; characteristic values are 10 m yr^{-1} in the downstream direction.

In figure 4.2 contour plots are shown of the first three most preferred cross-shore modes for $\gamma = 1.0 \times 10^{-4}$. The ridges appear to be rotated upcurrent, ie. their seaward ends are shifted upstream with respect to their shoreface attachments. Furthermore an offshore deflection of the current over the bars is observed. All these properties are in good agreement with those of observed shoreface-connected ridges (cf. Swift *et al.*, 1978; Van de Meene, 1994).
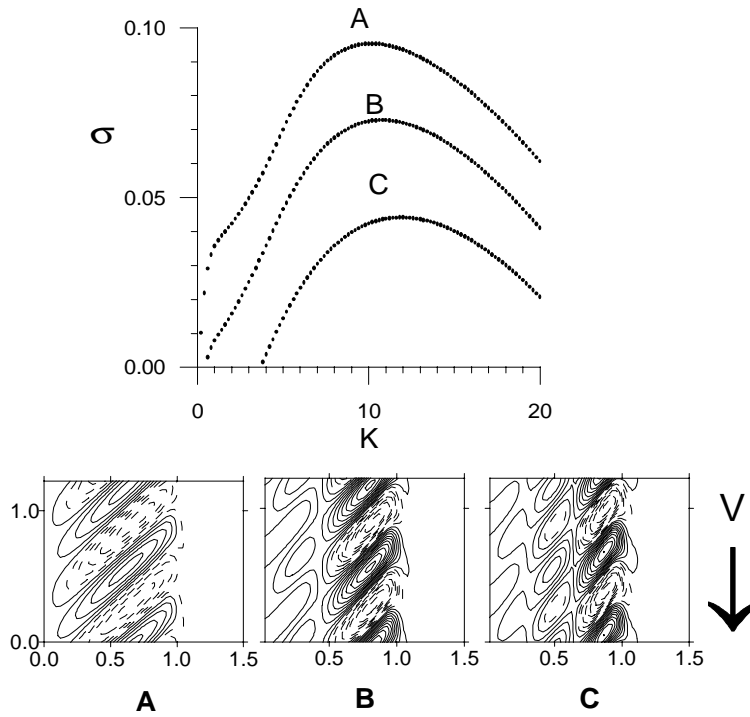
Figure 4.2: Nondimensional growth rate, $\sigma = \mathrm{Re}(\omega_{k\,n_k})$ as a function of the wavenumber, k, for the first three cross-shore modes, $n_k = 1, 2, 3$ (upper part). Parameter values are $r = 1.5$, $\hat{f} = 5.35$, $\gamma = 10^{-4}$, $\beta = 0.33$ and $V < 0$. The corresponding contour plots of the bottom perturbations are shown. Shoals and troughs are indicated by solid and dashed lines, respectively. In each plot the y axis (vertical on the left) represents the shoreface and the horizontal axis is the x-axis, with $x = 1$ the transition from inner to outer shelf. The direction of the basic current is shown by a big arrow. Note the upcurrent rotation of the ridges.

The dependence of the growth rate on the bed slope coefficient γ for the most unstable cross-shore mode is shown in figure 4.3. It shows that for values of the bed slope coefficient larger than a critical one, $\gamma_c \approx 10 \times 10^{-4}$, the basic state is linearly stable. For $\gamma < \gamma_c$ the the basic state is linearly unstable. Decreasing from γ_c the value of this diffusive parameter, the growth rate increases and the longshore wavelength of the preferred mode becomes longer.

As already has been pointed out in chapter 2 and by Trowbridge (1995) the mechanism which causes the growth of the ridges is related to the transverse slope of the inner shelf. Water columns moving over an upcurrent rotated ridge are deflected offshore, because due to mass conservation the velocity perpendicular to the crest increases if water depths become smaller. Due to this offshore deflection the water column will expand and experience a mass deficit. This is compensated for by a convergence in the flow velocity, causing a convergence in the sediment transport, since the latter depends linearly on the flow. As a result there is accumulation of sediment in the crest area, hence the bed form will grow.

Finally we remark that, although the linear stability analysis yields quite satisfactory results, it is subject to the limitation that it only describes the initial formation of bed form with a very small amplitude. Due to the transverse slope instability mechanism, the perturbation grows exponentially in time. However, after some time finite-amplitude effects will become important. Consequently, nonlinear terms in the equations of motions for the perturbation, which are neglected in a linear stability analysis, will become important. This motivates the study of a nonlinear mode which will be discussed in the next section.

Non-linear analysis: formulation

The nonlinear theory provides the tool to examine the long-term evolution of the shoreface-connected ridges with finite amplitudes, which will allow for a closer comparison between model
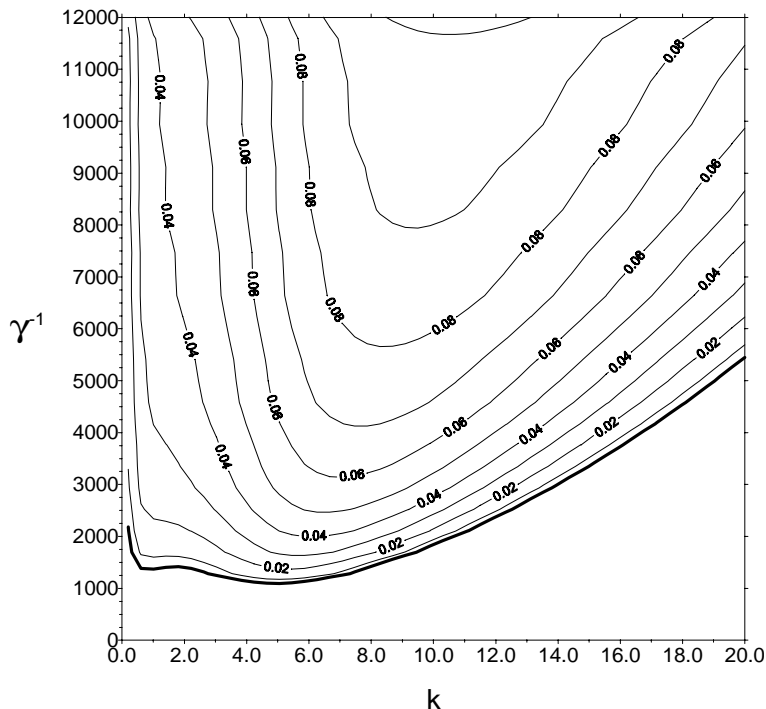
Figure 4.3: Contour plot of the growth rate of the first cross-shore mode as a function of wavenumber k and of the bed slope coefficient γ. All other parameter values are $r = 1.5$, $\hat{f} = 5.35$, $\beta = 0.33$ and $V < 0$.

results and field data. Because of the resemblance between the eigenfunctions of the linear problem and the observed ridges, and following Schuttelaars (1997), the nonlinear solution of the complete system (4.5)-(4.6)-(4.7) is expanded in terms of the linear eigenfunctions. This method has the considerable appeal of using actual linear solutions as a basis -rather than, say, some arbitrary polynomial- so that relatively few terms are necessary to describe the nonlinear evolution accurately. In addition, the use of the eigenfunction of the linear problem can be combined with the knowledge of the physical mechanisms, analyzed in chapter 2, in order to understand the physical processes.

The non-linear time-dependant solution $\Phi(x, y, t)$ is expanded as

$$\Phi(x, y, t) = \sum_k \sum_{n_k} \begin{pmatrix} \hat{u}(t)u(x) \\ \hat{v}(t)v(x) \\ \hat{\eta}(t)\eta(x) \\ \hat{h}(t)h(x) \end{pmatrix}_{k\,n_k} e^{iky} + \text{c.c.} \tag{4.9}$$

A standard method to derive the time evolution equations is to insert the expansion into the full nonlinear equations (4.8) and then to project the resulting equations onto the adjoint linear eigenfunctions. After defing the inner product and because of the quasi–steady hypothesis, only the component of bottom modes of the eigenfunctions $(h_{kn_k}e^{iky})$ are orthogonal to their adjoint $(h^+_{kn_k}e^{iky})$, see appendix F.1. A first set of equations come from the projection equation (4.7) onto the adjoint linear eigenfunctions of the bottom. To complete the system, equations (4.5) and (4.6) should be used. The projections over these equations is arbitrary and the adjoint linear eigenfunctions of the hydrodynamic variables are used. Following this Galerkin method, the equations for the amplitudes of each magnitude and mode kn_k read

$$0 = (u^+_{kn_k}e^{iky}, \mathcal{L}_u\Phi) + (u^+_{kn_k}e^{iky}, \mathcal{N}_u(\Phi)) \tag{4.10a}$$

$$0 = (v^+_{kn_k}e^{iky}, \mathcal{L}_v\Phi) + (v^+_{kn_k}e^{iky}, \mathcal{N}_v(\Phi)) \tag{4.10b}$$

$$0 = (\eta^+_{kn_k}e^{iky}, \mathcal{L}_\eta\Phi) + (\eta^+_{kn_k}e^{iky}, \mathcal{N}_\eta(\Phi)) \tag{4.10c}$$

$$(h^+_{k\,n_k} e^{\mathrm{i}k\,y}, \mathcal{S}_h \Phi) = (h^+_{k\,n_k} e^{\mathrm{i}k\,y}, \mathcal{L}_h \Phi) + (h^+_{k\,n_k} e^{\mathrm{i}k\,y}, \mathcal{N}_h(\Phi)).\qquad(4.10\mathrm{d})$$

Linear and nonlinear terms of equation (4.5a) are denoted in equation (4.10a) by $\mathcal{L}_u\Phi$ and $\mathcal{N}_u(\Phi)$, respectively. The same terminology is used for the other equations. In appendix F.2 equations (4.10) are explicitly written.

The first right terms of this system of equations are linear in the amplitudes $(\hat{u}, \hat{v}, \hat{\eta}, \hat{h})_{k\,n_k}$. Thus, the system can symbolically be written as

$$0 = L_1 U + M_1 h + f(U, h)\qquad(4.11\mathrm{a})$$

$$S\frac{\mathrm{d}h}{\mathrm{d}t} = L_2 U + M_2 h + g(U, h)\qquad(4.11\mathrm{b})$$

where h is a vector with components $\hat{h}_{k\,n_k}$ of the bottom perturbation and U represents the flow variables $(u, v, \eta)_{k\,n_k}$. Furthermore, f and g are vectors with components which are known nonlinear functions of the components of U and h.

The model is truncated in three ways: in the x and y coordinates, in time and in the expansion (4.9). The discretization in the x direction has been done by means collocation methods. The accuracy of the approximation is controlled by the number of collocation points and 80 points are usually enough. Because the dimension of the linear problem is proportional to the number of collocation, the number of eigenvalues are proportional to the number of collocation points. In the y direction a normal modes expansion, ie. Fourier Galerkin, method has been used. The time discretization is discussed in the appendix F.3.

The truncation of the expansion (4.9) is a crucial aspect of the model. Minimizing the number of modes (k, n_k) used in (4.9) will provide us with a more efficient and numerically stable code, as wil be shown later on. Furthermore, by reducing the dimension of our complex problem we gain physical insight. Nevertheless, this reduction should keep the physics of the problem. In order to carry out a proper truncation the eigenvalue spectrum has been analyzed. In the next section, detailed analysis of the solutions of the eigenvalue problem and an explanation of the criteria used to truncate the expansion (4.9) will be given.

Non–linear analysis: truncation

Characteristics -growth rate, migration speed and spatial structure- of the eigenfunctions of the linear problem and their dependence in kn_k should be analysed in order to find objective criteria to apply to the truncation in (4.9). As illustrated in figure 4.4, different behaviours of the growth rate curves are found, depending on the value of the cross-shore modenumber, n_k. In figure 4.5 a plot of the growthrate, $\sigma = Re(\omega_{k,n_k})$, is shown as a function of n_k for a fixed wavenumber k. It can be seen that the thick black line in figure 4.4 is the accumulation of eigenvalues with equal real and imaginary values (modes $n_k = 5$ to ≈ 30). Furthermore the crossing of modes in figure 4.4 corresponds not only to modes with different k dependence but also, see figure 4.5, to different n_k dependence of the migration speed c. There appear to be three different types of modes: a first set of modes with $|c|$ considerably smaller than 1 (modes $n_k = 1$ to $n_k = 5$, $n_k = 34, 41$) that will be named by modes type I, another group with $|c| = 1$, type II, and the rest of teh modes which $|c|$ have other slightly smaller than 1, type III. This classification from the migration speed is also coherent with the spatial structures these modes as we will see.

The first six type I modes are inner shelf modes. The contour plots of the bottom eigenfunctions, ie. the bottom perturbations, of these modes are shown in figures 4.6, 4.7 and 4.8. They appear to be the first six modes of upstream rotated ridges. Modes type II manifest themselves on the outer shelf and they are longshore perpendicular series of shoals and pools, figure 4.7. From their dependence on k (figure 4.4) and γ, $Re(\omega_{k,n_k})$ is proportional to γk^2, these eigenfuctions come from the diffusive term $-\gamma |V| \partial^2_{yy} h$ in the linear equation for the bottom, and, therefore, they are interpreted as diffusive modes. Figure 4.8 shows contourplots of modes which are called type III-modes. They have even smaller -more negative- growth rates; they resemble a mixture of diffusive and frictional and Coriolis modes, see chapter 2. Figure 4.5, where $\omega_{k n_k}$ is plotted as a function of n_k for $k = 40$, shows that for other wavenumbers k, although the migration speeds become closer to each other, a similar distribution of the eigenvalues is found. Their eigenfunctions are plotted in figure 4.9. Comparing figures of 4.5 we can see that for a fixed n_k a mode can change its type
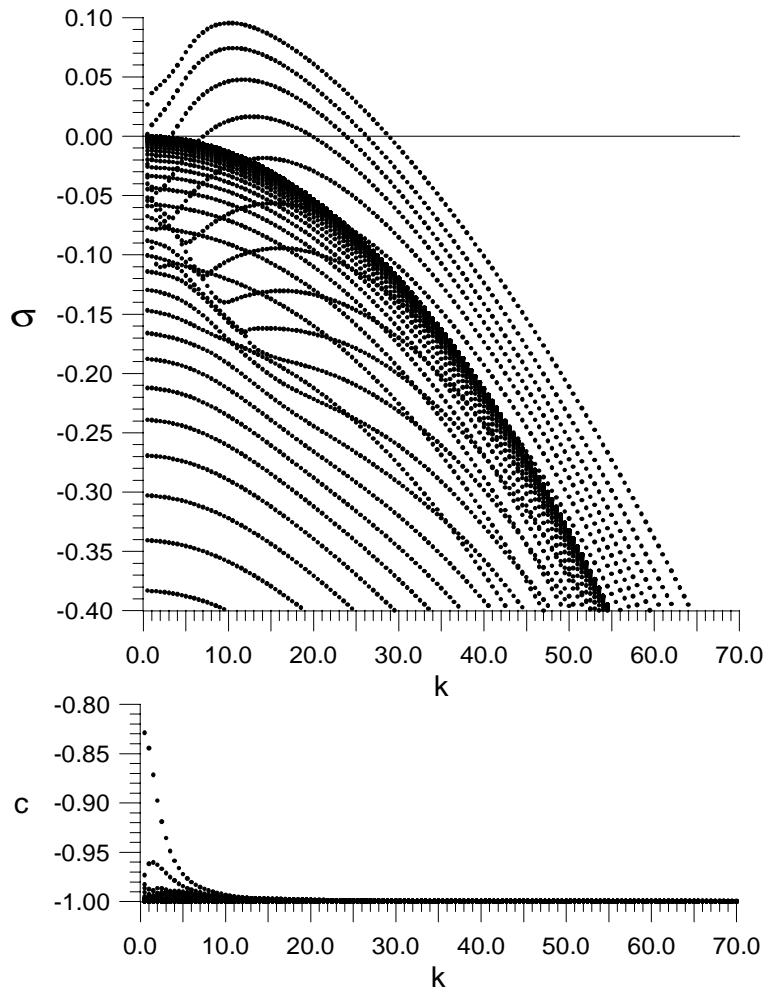
Figure 4.4: Nondimensional growth rate, $\sigma = \mathrm{Re}(\omega_{k\,n_k})$ and migration velocity, c, as a function of the wavenumber, k, for different cross-shore modenumbers n_k. Parameter values are $r = 1.5$, $\hat{f} = 5.35$, $\gamma = 10^{-4}$, $\beta = 0.33$ and $V < 0$.

if the wavenumber k is varied. For instance for $k = 10$ node $n_k = 31$ is a type II-mode while for $k = 40$ is a type I-mode.

Since diffusive modes mainly occur on the outer shelf they do not project onto the modes in the inner shelf and vice versa. The higher n_k modes have growth rates much smaller than the upstream rotated ridges. Therefore, only upstream rotated ridges will be used in the expansion (4.9).

The selection of the n_k modes of type I will be done using the difference in the migration speed c. This criterion, although clear for the modes with low n_k, is not specific enough for the higher ones; therefore it limits the number of n_k modes that would be used. In the same way, it is important to note that an increase of the resolution in the cross shore direction would increase the number of eigenvalues. Most of these eigenvalues will appear as diffusive modes (type II), but some eigenvalues will correspond to the complex modes (type III) with migration velocities and growth rates similar to the high n_k upstream ridges. This further complicates an objective choice of the eigenfunctions. On the other hand, for a numerically stable and correct solution a high number of collocation points is required by the computations. These two facts constrain us to deal with the number of collocation points and the necessity of distinguishing the different modes.

Expansion (4.9) is also truncated in the number of wavenumbers (Fourier modes) used. Only the mode with wavenumber K_M, having the largest initial growth rate (maximum in figure 4.3 for each γ) and its superharmonics will be used. This means that the computations are carried out in a longshore box of length $L = 2\pi/K_M$. As a first approximation, the $k = 0$ mode is not used; a justification of this is given in appendix F.4. The eigenfuctions in the expansion will be
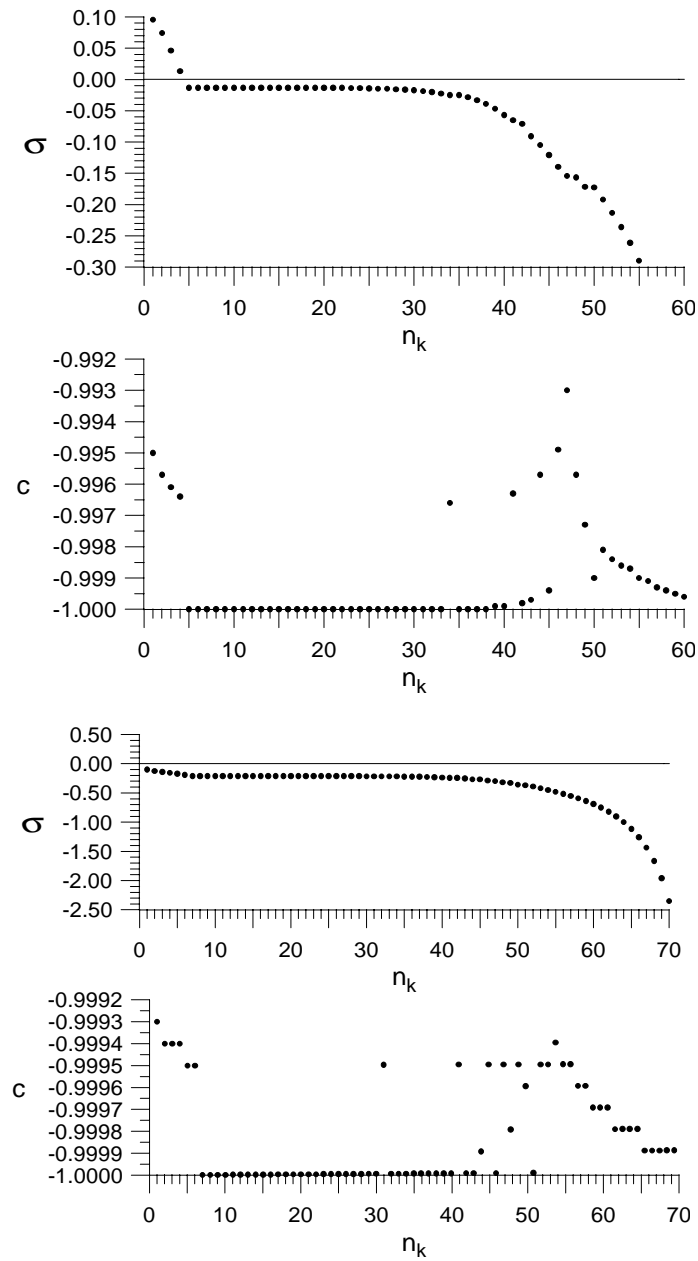
Figure 4.5: Nondimensional growth rate, $\sigma = \mathrm{Re}(\omega_{k\,n_k})$ and migration velocity, c, for $k = 10.0$ (top) and $k = 40.0$ (bottom), as a function of n_k. Parameter values are the same as in figure 4.4.
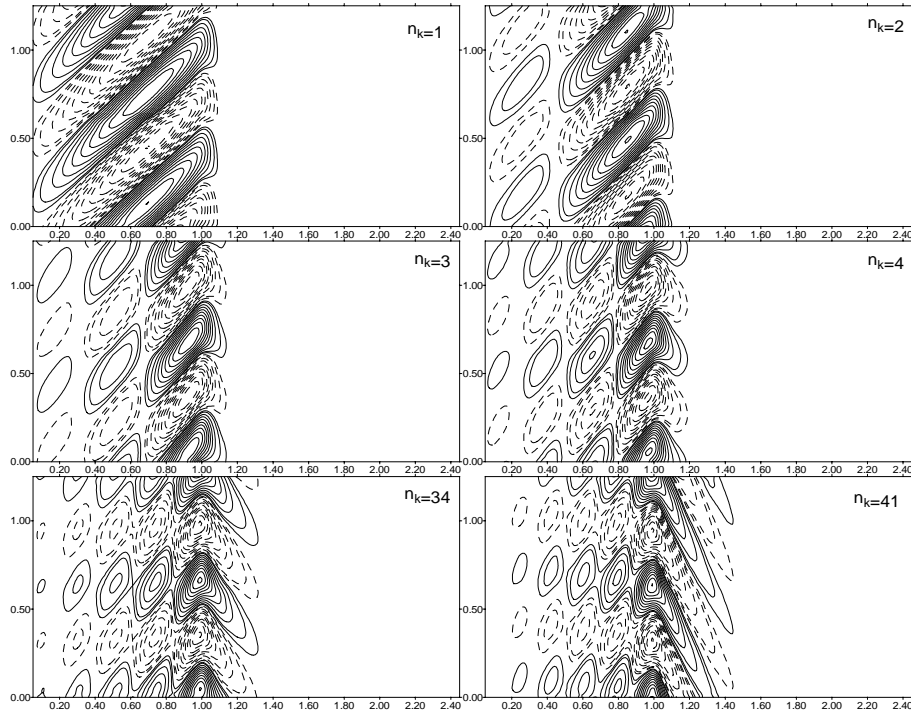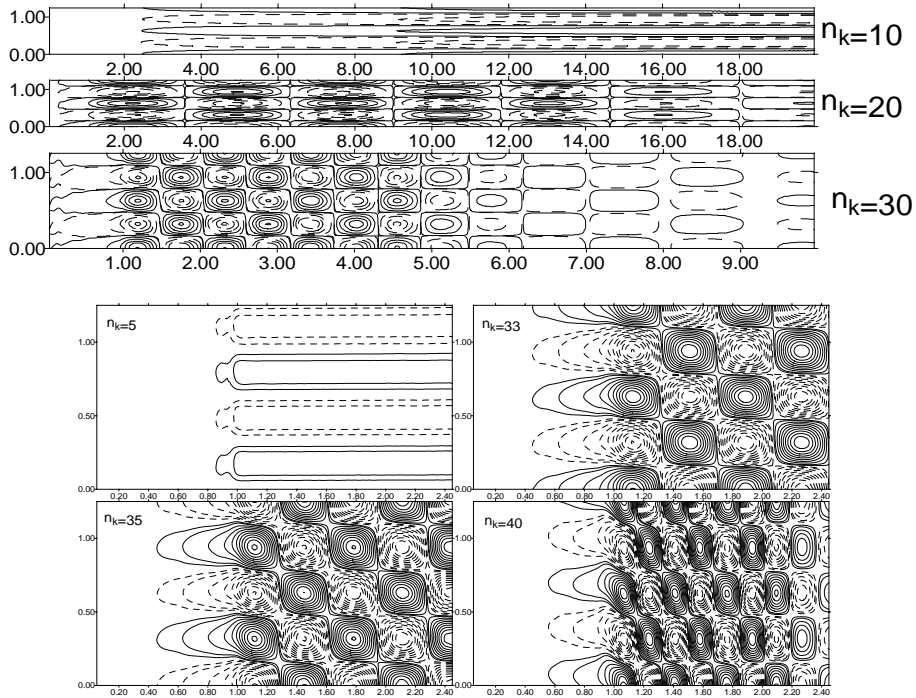
Figure 4.6: Contour plots for type I modes.

Figure 4.7: Contour plots for type II modes.

denoted by a pair (j, n_j); the first symbol, j, corresponds to the number of the longshore mode $(k = K_M \rightarrow j = 1$, $k = 2\,K_M \rightarrow j = 2$, ...) and the second one, n_j, refers to the cross-shore structure of the retained modes used in the expansion. For example, in case of $\gamma = 1.0 \times 10^{-4}$ the most unstable mode is $K_M = 10$, so the upstream rotated ridge of $k = 40$ and $n_k = 31$ of figure 4.9
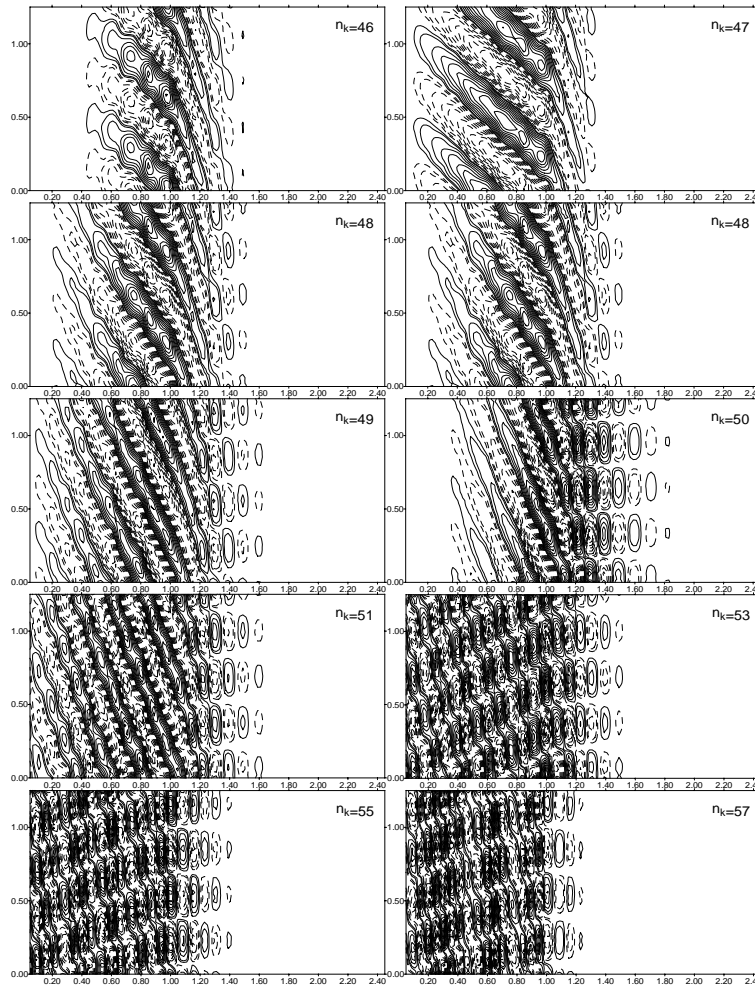
Figure 4.8: Contour plots for type III modes.

is renamed as (4,7). After these considerations, the expansion (4.9) for the type I modes is

$$\Phi(x,y,t) = \sum_{j=1}^{J} \sum_{n_j=1}^{N_J} \begin{pmatrix} \hat{u}(t)u(x) \\ \hat{v}(t)v(x) \\ \hat{\eta}(t)\eta(x) \\ \hat{h}(t)h(x) \end{pmatrix}_{jn_j} e^{ijK_M y} + \text{c.c.}, \tag{4.12}$$

where J is the number of Fourier modes and N_J the number of cross-shore modes for each j. This notation will be used in the next section. Furthermore, the number of collocation points used in the discretization of the x–coordenate will be denoted by N_x.
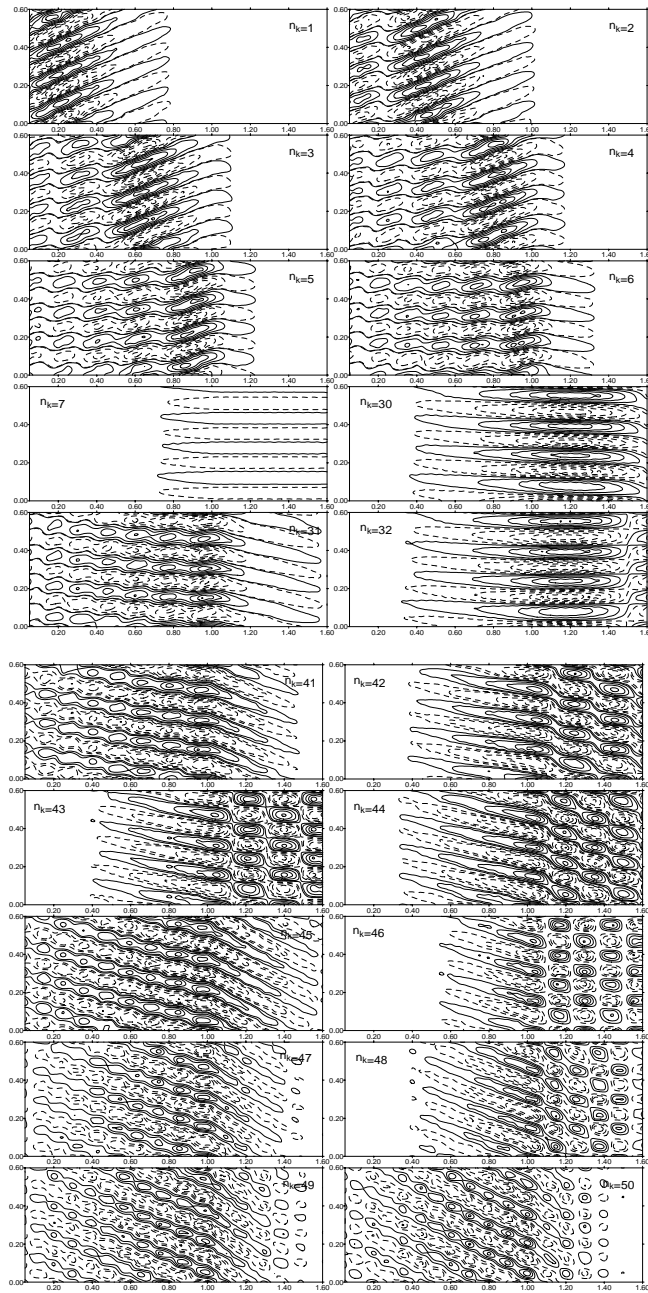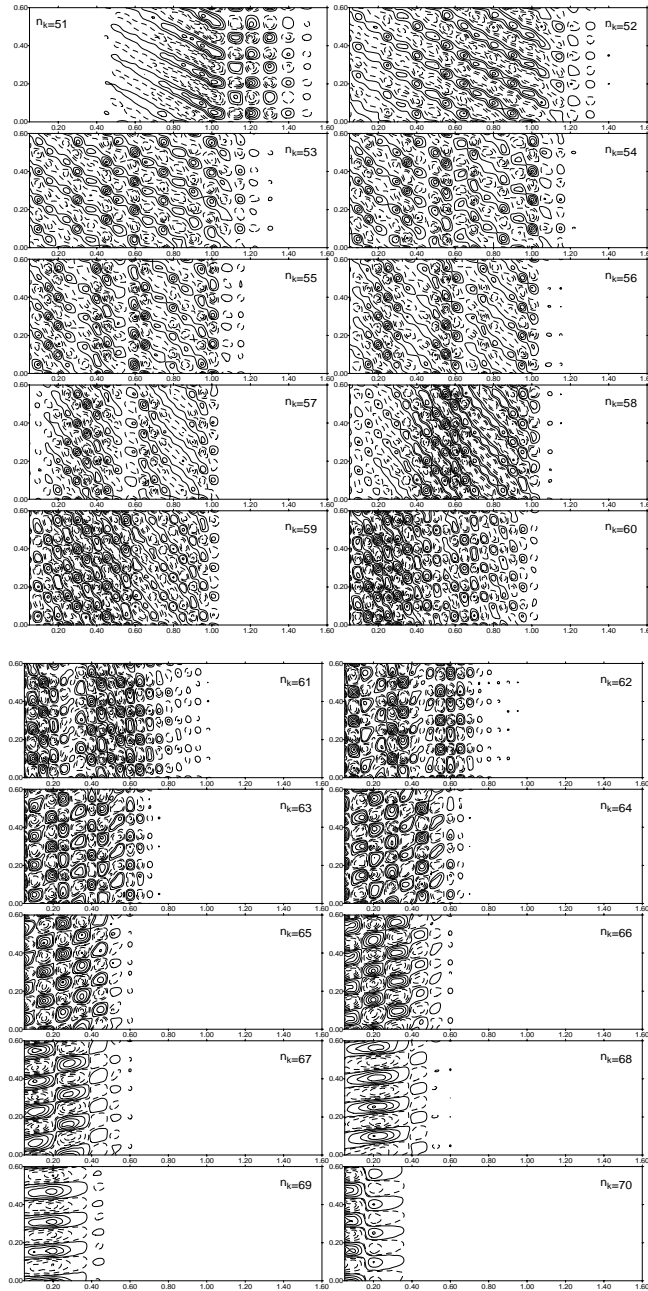
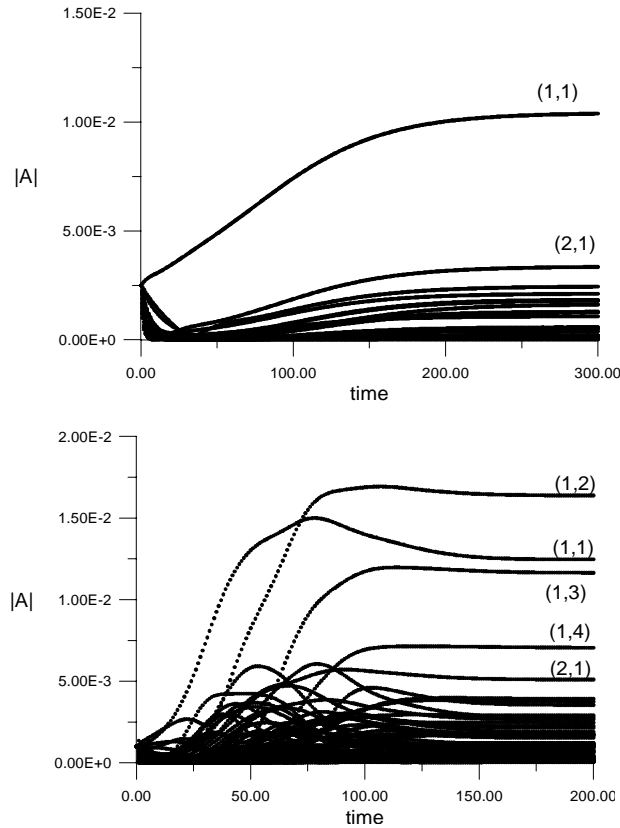Figure 4.9: Eigenfunctions for $k = 40$ (figure 4.5 bottom).

Figure 4.10: Example of time evolution of the amplitude of the different bottom modes. **Top**: $\gamma = 8.0 \times 10^{-4}$ and the truncation parameters are $K_M = 5.3$, $N_x = 100$, $J = 5$, $N_J = 4$. **Bottom**: $\gamma = 2.0 \times 10^{-4}$ and $K_M = 8.3$, $N_x = 100$, $J = 15$, $N_J = 7$.

4.3   Results: nonlinear model

The results of the nonlinear model for different values of the γ parameter are shown in this section. The number of superharmonics, J, used depends on the γ parameter; with decreasing γ the basic state becomes more unstable, so more superharmonics are needed. Since the complexity of the final solution also increases with decreasing γ, more cross-shore modes, N_J, are needed in that case. For $\gamma > 4.0 \times 10^{-4}$, 5 Fourier modes in the longshore direction and 4 modes in the cross-shore direction are sufficient in the sense that results remain unchanged if the number of modes in either direction is increased. Instead, for smaller values of γ the model becomes very sensitive to the number of modes used and 20 Fourier modes and 8 cross-shore modes are needed. The computations have been done with 100 collocation points in the discretization of the cross-shore direction. The time integration scheme to solve the coupled system of algebraic and differential equations (4.11) is shown in the appendix F.3. The time integration has been carried out with a time step $\Delta t = 10^{-3}$ morphological units in a third order scheme. As initial conditions, in the numerical experiments all the modes have the same initial amplitude which is between 1.0×10^{-3} and 2.5×10^{-3}. For large γ ($9.5 \times 10^{-4} - 4.0 \times 10^{-4}$) the final state does not depend on this initial amplitude but for smaller γ values the model behaviour starts to depend on the initial condition.

Numerical experiments for γ slightly larger than $\gamma_c \simeq 10 \times 10^{-4}$ show agreement between the linear and the nonlinear analysis in the stability of the basic state, i.e, the amplitude of all the modes tend to zero. For values of $\gamma = 9.5 \times 10^{-4} - 4.0 \times 10^{-4}$ the $(1,1)$ mode is the mode with the highest amplitude. The time evolution of the modal amplitudes and the bottom perturbation for $\gamma = 8.0 \times 10^{-4}$ is shown in figures 4.10 and 4.11. If the initial amplitude of the perturbation is very small, the initial growth is exponential, followed by saturation. If the initial amplitude is larger, the system evolves to the same final state, no matter which initial conditions have been taken. The migration speed of the modes does not differ from its corresponding velocity in the
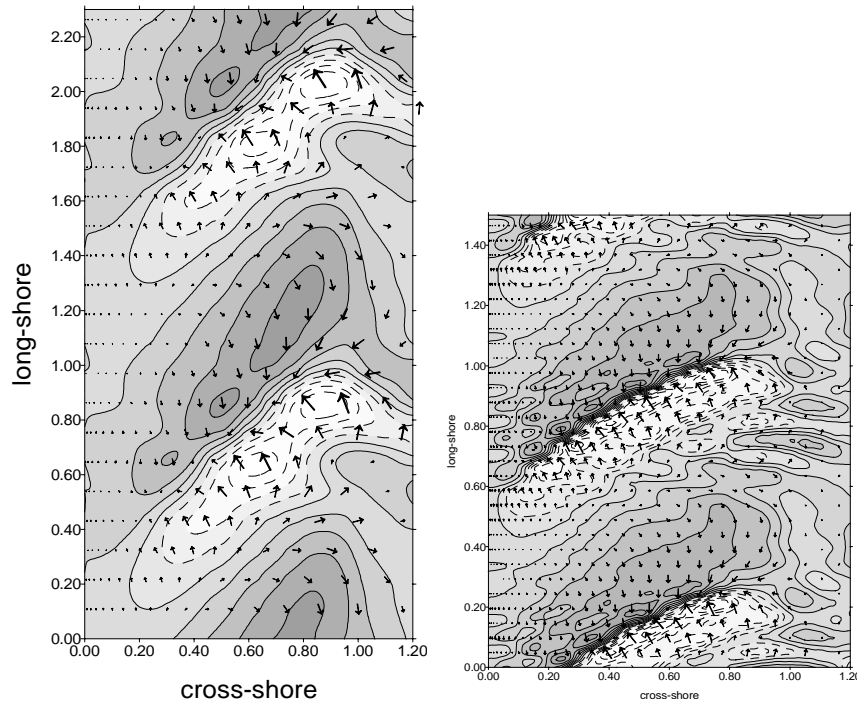
Figure 4.11: Topographic perturbation and flow perturbation for $\gamma = 8.0 \times 10^{-4}$ (left) and $\gamma = 2.0 \times 10^{-4}$ (right) of figure 4.10. Shoals in dark, troughs in white.
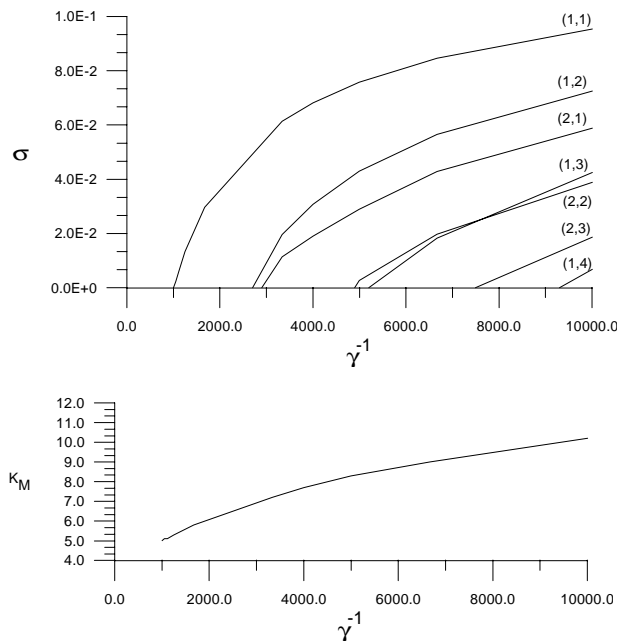

Figure 4.12: **Top:** Nondimensional growth rate of the modes (j, n_j) unestables as a function of the bed slope parameter, γ. **Bottom:** K_M as a function of the bed slope parameter.

linear problem, which is close to -1.

By decreasing γ to more realistic values, more modes become linearly unstable and K_M becomes larger, see figure 4.12. For small γ, higher cross–shore modes in $k = K_M$ ((1,2), (1,3)...) grow in time even to final amplitudes which are larger than the final amplitude of the linearly dominant mode, (1,1). This can be seen in figure 4.13.

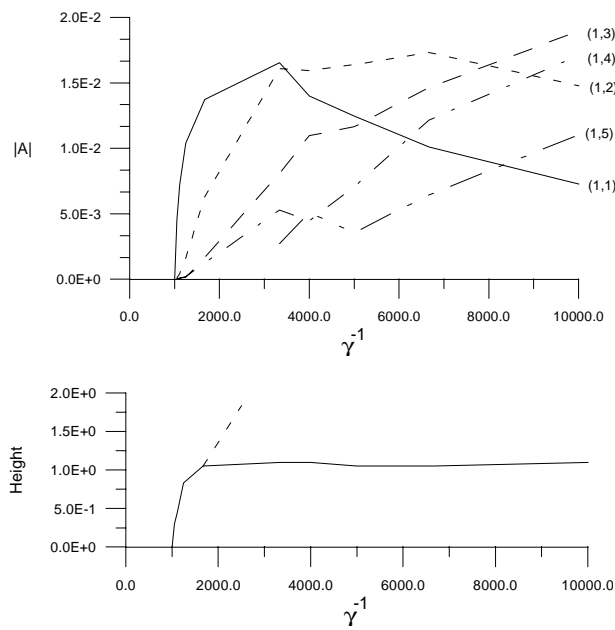The time evolution of the mode amplitudes and the final bottom and velocity perturbation for

Figure 4.13: **Top:** Final amplitude of the different bottom modes as a function of the bed slope parameter, γ. **Bottom:**Height of the bed forms (in m) as a function of γ.
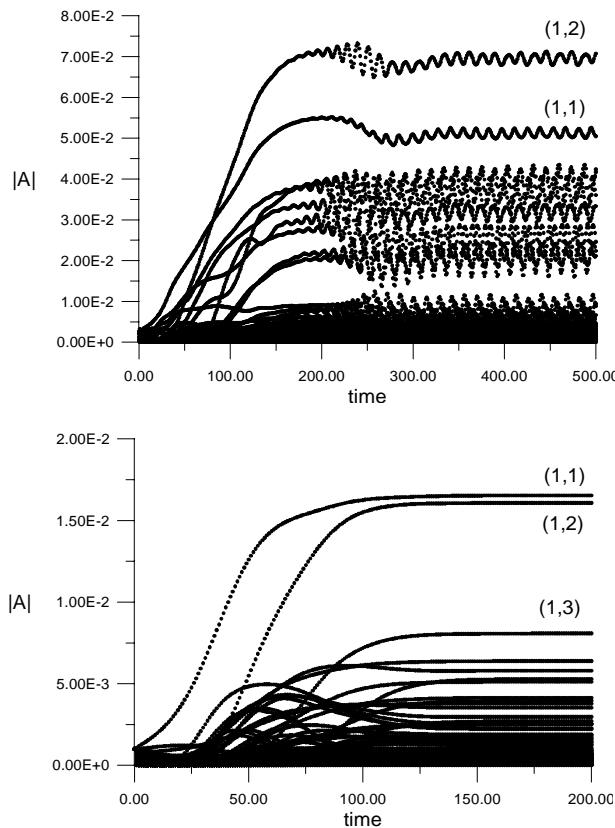

Figure 4.14: Time evolution of the amplitude of the different bottom modes for $\gamma = 3.0 \times 10^{-4}$, i the top for the higher (high-amplitude) and in the bottom for lower branch (low-amplitude) of figure 4.13. Note that the scale of both the horizontal and vertical axes is different.

$\gamma = 2.0 \times 10^{-4}$ are shown in figure 4.10 and 4.11. The perturbed topography shows a complexity which is not displayed by any of the individual eigenmodes of the linear problem and is much more
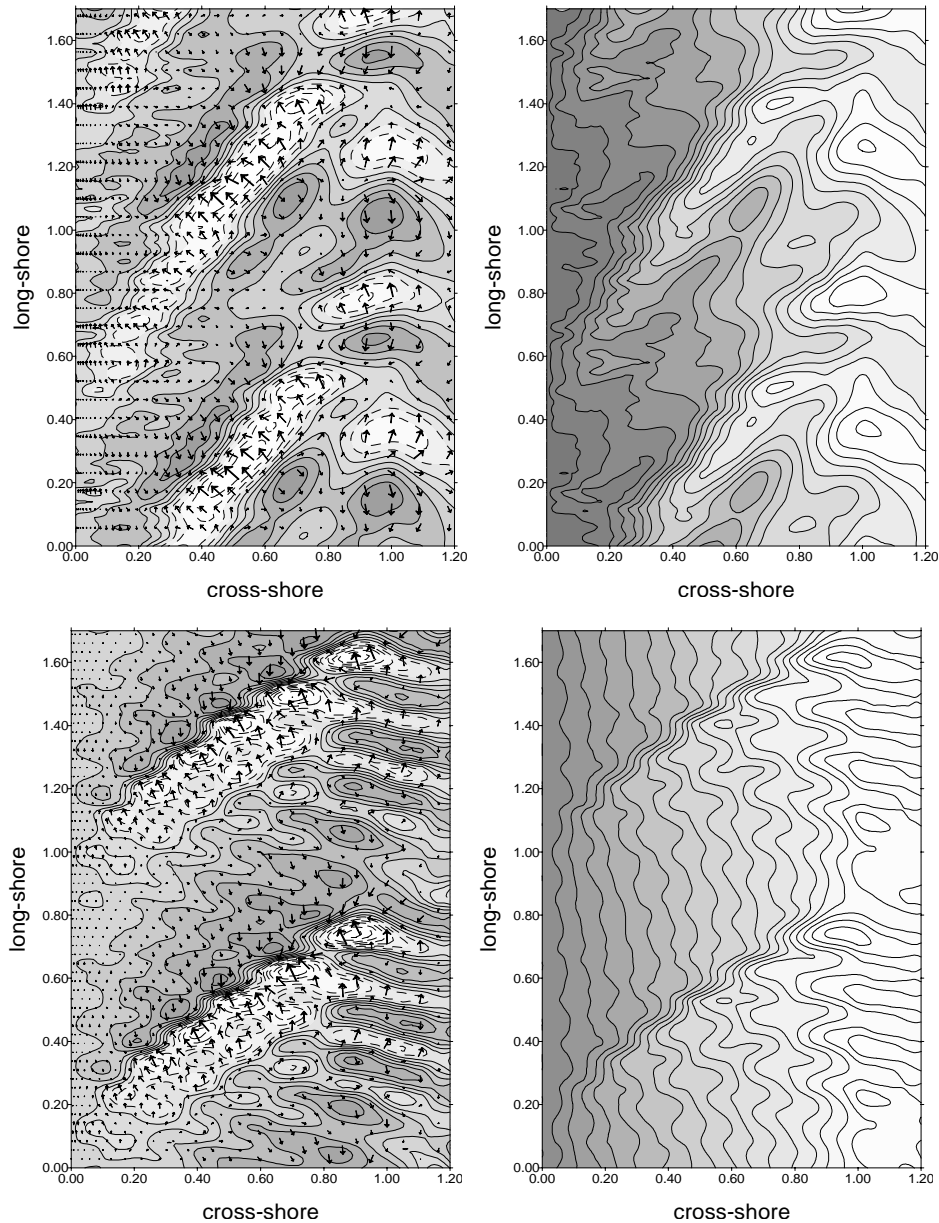
Figure 4.15: Perturbation of the bottom and total depth for the upper branch (top) and lower branch (bottom). Shoals in dark, troughs in white.

similar to the observed topographic patterns. For instance, secondary shoals and dislocations of the main sand bank occur. A typical nonlinear effect which is observed is a clear asymmetry along the current: the slope on the lee side is much pronounced than the slope in the stoss side. It is also important to remark that the flow velocity perturbation is slightly accelerated and deflected in the offshore direction, whereas over the troughs the flow is strongly curved and deflected inshore.

The height of the bed forms is of the order $1 - 2$ m in accordance with observations on the Dutch coast. As it can be seen in figure 4.13, it does not change very much by changing γ, except for γ close to γ_c where the total amplitude is proportional to $(\gamma^{-1} - \gamma_c^{-1})^{1/2}$. This dependence on the control parameter γ^{-1} of the amplitude of the periodic solution is what is expected from the bifurcation theory in case of a Hopf bifurcation (see e.g. Guckenheimer & Holmes, 1983).

A second bifurcation has been found for $\gamma \simeq 3.0 \times 10^{-4}$ (ie. $\gamma^{-1} \simeq 3000$). Time evolution of the amplitudes for both branches at $\gamma \simeq 3.0 \times 10^{-4}$ are shown in figure 4.14. The numerical experiment of lower branch of figure 4.13 at $\gamma \simeq 3.0 \times 10^{-4}$ has been done with $N_x = 100$ and for $K_M = 7.2$, $J = 15$ and $N_J = 7$. For the upper branch $N_x = 60$, $K_M = 7.2$, $J = 15$ and for

$N_1 = 6$, $N_2 = 5$ and for $J = 3 \div 15$, $N_J = 4$. The amplitudes $|A|$ of each mode of upper branch are modulated in the long term, then at least in two frequencies the solution depends; one related with the migration and the other with the modulation. These two frequencies seem to have an irrational ratio. In figure 4.15 the perturbation of the bottom and total depth corresponding to the two branches are plotted. Both solutions look like upstream rotated ridges, but differ in the height of the perturbation and in the flow structure. The amplitudes of the upper branch are large enough to be an appreciable proportion of the total depth, something that does not hold for the lower branch solution. The amplitude of the solution is not the only difference; in the upper branch the bottom mode with the larger amplitude is mode (1,2) while for the lower is the mode (1,1). Also the flow over the ridges appears to be different. The appearance of two types of solutions allows us to suggest that several unstability or saturation mechanisms are competing in the model. However, in this parameter range the model behaviour is very sensitive to the initial conditions and to the discretization parameters (number of longshore and cross-shore modes) so that a more systematic analysis is required. The experiments for $\gamma < 2.0 \times 10^{-4}$ correspond to the lower branch.

In some of the previous figures, time evolution of the bottom amplitudes has been shown; it is also interesting to look how the perturbations of the bottom and the flow evolves in time. An example of this time evolution for $\gamma = 8.0 \times 10^{-4}$ and $\gamma = 2.0 \times 10^{-4}$ is shown in figures 4.16 and 4.17, respectively. The amplitude behaviour of the different bottom modes as a function of time are shown in figure 4.10. For instance, in figure 4.17 can be seen that from $t = 0$ to $t = 75$ bottom perturbations grow and the flow is deflected in the offshore direction over the ridges, as the linear stability analysis predicts. At the final saturated state the offshore deflection is also present. Both in the transient and in the final state the migration of the bottom modes has the same speed as the linear modes. At the final state the amplitude of the bottom pertubation is 1 m and the deviation of the velocity is about 10%. The maximum variation in the depth and the flow velocity is between the crest and the adjacents trough.

It is important to note that the time unit is the morphodynamic one which, for a migration speed of $10 \, \mathrm{m \, yr^{-1}}$ is $T_m = 1000$ yr. Because the time that the bedforms need to grow significantly is of the order of $100 \, T_m$ the results only make sense as a continuation in the γ parameter. A way to reduce this evolution time to a more realistic one is to increase the initial amplitude of the perturbation. This can be done for large values of γ with the result that the time is reduced to order of a few times T_m. However, for more realistic values of γ ($\gamma = 1.0 \times 10^{-4}$) a larger initial amplitude makes the model numerically unstable. Finally it should be remarked that numerical experiments without filtering the diffusive modes have been carried out; all these experiments not only need too much time for each time step but it also produce a strong numerical unstability the model.

4.4 Conclusions

In this chapter a nonlinear morphodynamic model has been analyzed to gain more fundamental knowledge about the initial and long-term behaviour of observed shoreface-connected sand ridges. The model describes quasi-steady, depth-averaged flow on a storm-dominated inner shelf with an erodible bottom and a transverse slope. A local parametrization for the sediment transport is used, which is assumed to be linear in the current and accounts for the effect of local bedslopes.

A linear stability analysis has revealed that the initially formation of bed forms is very similar to the observed shoreface-connected ridges which can be described as an instability of the coupled water-bottom system. The most preferred bottom modes have characteristic longshore wave-lengths of $5 - 8$ km, and they migrate in the downstream direction with a velocity of about $10 \, \mathrm{m \, yr^{-1}}$. The bed forms are trapped on the inner shelf and the seaward end of the crest are rotated upstream with respect to their sore face attachments. The growth is triggered by the transverse slope of the inner shelf which causes accumulation of sediment in the ridge area for offshore directed flow. The latter condition only occurs for upcurrent-rotated bars.

A limitation of the linear stability analysis is that it does not yield information about the finite-amplitude behaviour of the ridges. Hence, a nonlinear analysis has been carried out to study the long-term dynamics of the bed forms. This was done by expanding the flow and the bottom perturbations in a truncated series of eigenfuctions of the linear problem for a coastal stretch with
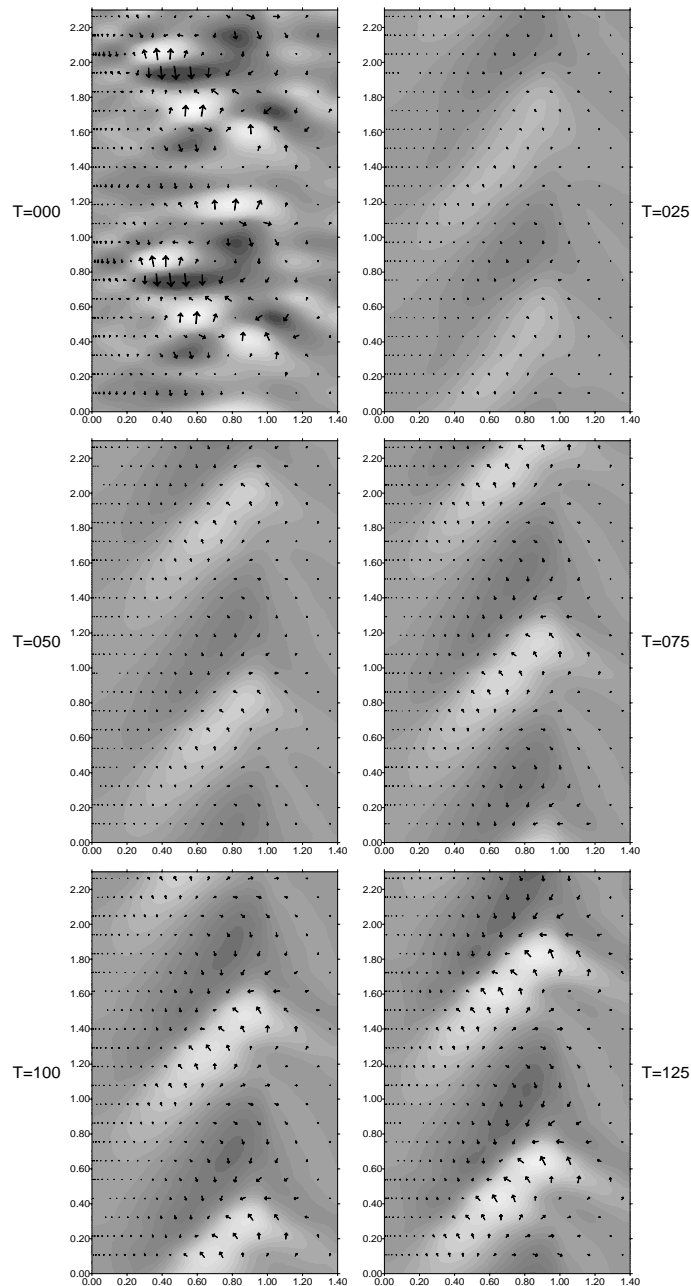
Figure 4.16: Time evolution of the bottom perturbation for $\gamma = 8.0 \times 10^{-4}$.

a fixed longshore length. The result is a set of nonlinear algebraic equations, describing the flow over the topography, and differential equations for the bottom amplitudes.

The robustness of the model is strongly related to the filtering of diffusive modes in the truncated eigenfunction expansions. If these modes are retained the model appears to be subject to numerical instabilities. This is due to the fact that the diffusive modes mainly occur on the outer shelf and therefore do not project well onto the relevant inner shelf modes; they become a source of numerical troubles and give a limitation on the parameter range where the model can be run. Therefore, it has been necessary to develop a numerical procedure in order to avoid the blow up of the model. The results appear to depend strongly on the number of modes which have initially positive growth rates, as controlled in the present experiments by the value of the bed slope coefficient in the sediment transport, γ. For large values of γ no bed forms develop and the reference state (which describes a longshore uniform flow over the transversely sloping shelf) is stable. If γ is decreased below a critical value γ_c there is one mode which initially amplifies. Due to nonlinear effects
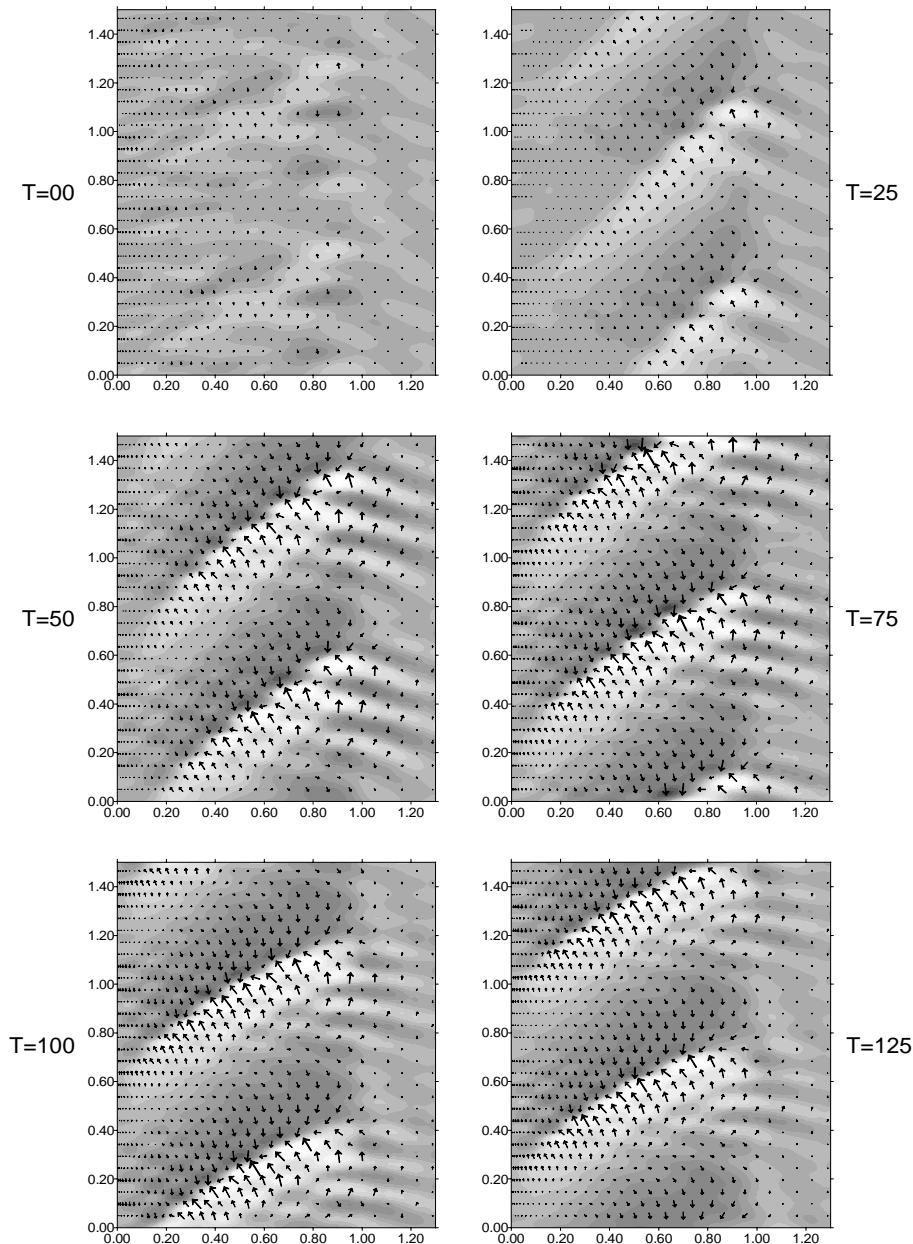
Figure 4.17: Time evolution of the bottom perturbation for $\gamma = 2.0 \times 10^{-4}$.

solutions starting from arbitrary initial conditions tend to a unique equilibrium. The latter is dominated by the initial most preferred mode and resembles a shoreface-connected ridge with an amplitude which scales like $(\gamma^{-1} - \gamma_c^{-1})^{1/2}$. A migration speed of this finite-amplitude perturbation appears to be unaffected by nonlinear effects. This is probably due to the fact that the dispersive properties of the linear perturbations are very weak.

If γ is reduced to even more realistic values more modes have initially positive growth rates and the model behaviour becomes rather complex. First results indicate that there are multiple attractors, in other words, the long-term behaviour depends on the initial conditions. It turns out that the final solutions are often dominated by a mode which is not the initially most preferred mode. There are also indications that the attractors have different properties. The 'low-amplitude' equilibrium describes a periodic bottom pattern whereas the 'high-amplitude' final state may show quasi-periodic behaviour. However, the latter case has to be studied in more depth, by including more eigenfuctions in the model to reach more definitive conclusions.

The spatial patterns of these final states have the typical characteristics of nonlinear features:

steep bottom gradients on the downstream side, the presence dislocations and the mixture of large-scale and smaller-scale patterns.

The overall conclusion is that the results obtained with the nonlinear model are very promising and may have important consequences for the interpretation of field observations near the shoreface-connected ridges. The model can also be used to get indicative information about the effect of the human interferences on the dynamics of these ridges and the implications for coastal stability.